Scattering Investigation of Multiscale Organization in Aqueous Solutions of Native Xanthan

Aristeidis Papagiannopoulos[1,*], Konstantinos Sotiropoulos[1] and Aurel Radulescu[2]

[1]Theoretical and Physical Chemistry Institute, National Hellenic Research Foundation, 48 Vassileos Constantinou Avenue, 116 35 Athens, Greece.

[2]Jülich Centre for Neutron Science JCNS Forschungszentrum Jülich GmbH, Outstation at Heinz Maier-Leibnitz Zentrum (MLZ), 1 Lichtenbergstraße, 85747 Garching, Germany.

Corresponding Author

E-mail address: apapagiannopoulos@eie.gr (A. Papagiannopoulos)

Abstract

The hierarchical morphology of xanthan solutions is analyzed by light scattering and small angle neutron scattering experiments in a broad range of concentrations. Static light scattering well inside the semi-dilute regime is dominated by the form factor of individual xanthan chains while at higher concentrations chain interconnections appear to modify the low wave vector scattering. Dynamic light scattering on the other hand reveals the self-similar nature of the solutions caused by interchain associations. Concequently intensity autocorrelation functions present power-law behaviour with exponents that decrease as a function of concentration. Small angle neutron scattering profiles are dominated by the fractal scattering from the formed network at intermediate length scales. At small length scales the data is consistent

with the rigid helical structure of xanthan molecules and hence the molecular weight per unit length is extracted. Measurments at shear rates up to 1000 rad/s caused no detectable conformational or morphological alterations to the scattering profiles revealing that the shear thinning behaviour of xanthan is related to the disruption of chain-chain associations. This study illustrates the use of scattering methods for analysing structure in complex fluids of interest in food and pharmaceutical industry.

Keywords: light scattering, small angle neutron scattering, xanthan, polysaccharide, fractal, helix.

1. Introduction

Xanthan is an anionic polysaccharide originated by the bacteria species Xanthomonas and produced commercially mainly by Xanthomonas campestris via fermentation process[1]. It consists of a cellulose backbone and trisaccharide side chains that include glucuronic acid groups, mannose units and pyruvate residues that provide its anionic charge[2]. In salt containing aqueous solutions the trisaccharide charged side chains of xanthan create stable helices along its backbone[3].Among its most interesting features some are the high viscosity even at low concentrations solutions, the stability in a wide range of temperatures, pH and salts, the ability to form hydrogels and the shear thinning behaviour. One of xanthan gum's main uses is that of viscosity stabilizer/modifier in the food industry in a wide variety of products. Other applications include pharmaceutical products (dental treatment gels, external analgesics, etc.), personal care (shampoos, sunscreens, etc.), drug delivery systems, especially in the form of complexes combined with the cationic polyelectrolyte chitosan[4] and oil recovery agents[5].

In our recent publication[6] we demonstrated the power-law viscoelasticity of xanthan solution at concentrations relevant to industrial applications. The connection of the linear rheology (obtained by particle tracking microrheology) with the shear-thinning behaviour (meassured by viscometry) was established. Xanthan has been studied in the past by static light scattering in dilute solution in terms of its wormlike conformation[7, 8]. Its persistence length, molecular mass and molecular mass per unit length have been quantified. Dynamic light scattering studies have been performed performed to elucidate the diffusion coefficient as a function of concentration[9] at several salt conditions[10]. In these studies the apparent diffusion of xanthan molecules was found to depend on the effects of interchain interactions and cooperative motion above the overlap concentration.

Self-similarity in dynamic properties are intuitevely connected to self-similarity in spatial morphology[6, 11]. The well documented power-law viscoelasticity of xanthan solutions should be expected to reflect on its underlying structure. Both the dynamic and static scattering data would consequently contain the signature of self-similarity. In this study we use static and dynamic light scattering to elucidate the size and relaxation spectrum of xanthan molecules in semidilute solutions. We also probe the structure in a wide range of length scales by small angle neutron scattering and test the morphology under shear flow. This work extends the knowledge of xanthan morpholgy in semidilute solutions, sets a unifying framework for their description and can be generalized to complex fluids consisting of other biopolymers.

2. Materials and Methods

Materials

Xanthan gum was purchased from CP Kelco and was used without further treatment. The powder was dissolved in water under stirring in the desired concentration and

stored overnight at 4 ºC. Distilled H_2O was used for the light scattering experiments and D_2O for SANS experiments. Salt content was adjusted by adding small amounts of concentrated salt solutions (NaCl) up to the desired volume and the samples were again stored at 4º C overnight. The salt content was set at 0.03 M so that xanthan is in its ordered helical conformation[12, 13]. All measurements were performed at room temperature.

Light Scattering

Light scattering (LS) was performed on an ALV/CGS-3 compact goniometer system (ALVGmbH, Germany) equipped with an ALV-5000/EPP multi tau digital correlator and a He-Ne laser operating at the wavelength of 632.8 nm. In static light scattering (SLS) the Rayleigh ratio $R(q)$ was obtained at a series of angles in the range 30-120°. The scattering wave vector is given by $q = \frac{4\pi n_0}{\lambda} sin\frac{\theta}{2}$ where n_0 is the solvent's refractive index. SLS data were treated[14] by equation 1.

$$\frac{Kc}{R(q,c)} = \frac{1}{M_w P(q)} \qquad (1)$$

where M_w is the weight-averaged molar mass and c is the particle concentration in solution. In the Guinier approximation the single particle's form factor is given by $P(q) = e^{-\frac{1}{3}q^2R_g^2}$, where $R_g$is the radius of gyration obtained by SLS. K is the contrast factor for LS given by $K = \frac{4\pi^2 n_0^2}{N_A\lambda^4}(\partial n/\partial c)^2$, where $\partial n/\partial c$ is the refractive index increment of the scattering particles in the solvent. In dynamic light scattering (DLS) the intensity autocorrelation functions $g_{(2)}(t)$ were collected[15] at the same scattering angles as in SLS. The intensity autocorrelation function $g_{(2)}(\tau)$ is connected to the field autocorrelation function $g_{(1)}(\tau)$ by the Sieget relation $g_{(2)}(\tau) - 1 = \beta \cdot \left|g_{(1)}(\tau)\right|^2$ (where β is a normalization factor). CONTIN algorithm was used to extact the spectrum of relaxation times of the $g_{(1)}(\tau)$.

Small Angle Neutron Scattering

The KWS-2 high intensity/wide-q small angle neutron diffractometer at the research reactor FRM II (Jülich Centre for Neutron Science) was used for the small angle neutron scattering (SANS) experiments. The sample solutions were loaded in an Anton Paar (MCR 501) rheometer in the Couette geometry. This way SANS measurements under controled flow conditions (Rheo-SANS) were also possible. Scattered intensity was collected only in the radial direction. In the tangential geometry the requirement for narrow beam size compromised the incoming neutron flux significantly. The scattering vector (q) range was from 0.0022 to 0.3 $Å^{-1}$ and was covered by three separate sample-detector-distance/neutron-wavelength configurations i.e. 20m/0.5nm, 8m/0.5nm and 2m/0.5nm. Additionally the low q range could be extended to 0.0012 $Å^{-1}$ by measuring at 20m/1.0nm configuration.

In SANS the scattered intensity $I(\vec{q})$ is collected by a 2-D detector and is afterwards azimuthally integrated leading to the 1-D intensity $I(q)$. The 2-D raw data are corrected for the scattering from the empty cell and the solvent and the electronic and background noise. Intrumental resolution $\Delta q(q)$ is taken into account[16] by equation 2. The convoluted curves $I^{conv}(q)$ are the ones fitted against the experimentally obtained data $I^{exp}(q)$.

$$I^{conv}(q) = \frac{1}{\sqrt{2\pi}\Delta q(q)} \cdot \int_{-\infty}^{+\infty} dQ \cdot exp\left(-\left(\frac{Q-q}{\sqrt{2}\Delta q(q)}\right)^2\right) \cdot I^{th}(Q) \qquad (2)$$

Data fitting was performed by minimizing the sum of the weighted square differences $\chi^2 = \sum_{i=1}^{N}\left(\frac{I^{conv}(q_i)-I^{exp}(q_i)}{\delta I^{exp}(q_i)}\right)^2$ between the N theoretical and experimental data points for a SANS profile. The nonlinear least square optimization was performed by the Monte Carlo algorithm in a simulated annealing process[17] by custom made code in MATLAB.

3. Results and Discussion

Light scattering experiments covered a wide range of concentrations (0.03-1.4 mg/ml). In figure 1 we present the distribution of relaxation times from CONTIN analysis at 90°. At low concentration (0.03 mg/ml) a single broad peak is observed. This could be atributted to a single assumingly diffusive species with R_h about 80 nm a value somewhat lower than previously reported[10]. A high degree of polydispersity would explain the broad range of relaxation times. At intermediate concentrations (0.6 mg/ml) the distribution is apparently bimodal with the two main contributions being separated by more than one order of magnitude in time. At high concentrations (1 mg/ml) the distribution is apparently multi-modal spanning in more than five orders of magnitude in time. As we have recently shown[6] the range of concentrations above 0.05 mg/ml is well within the semidilute range of xanthan solutions. Additionally xanthan solutions have shown characteristics of self-similar structure as they resulted to power-law behaviour in viscoelasticity. They could hence be described as soft hydrogels on the critical point of gelation[11] where clusters of infinite correlation length are formed between xanthan molecules. Viscoelasticity in self-similar fluids is more naturally described by power-laws than with superposition of multiple modes. The power-law viscoelastic exponents of xanthan decreased systematically as a function of concentration pointing to the enhancement of the elastic component.

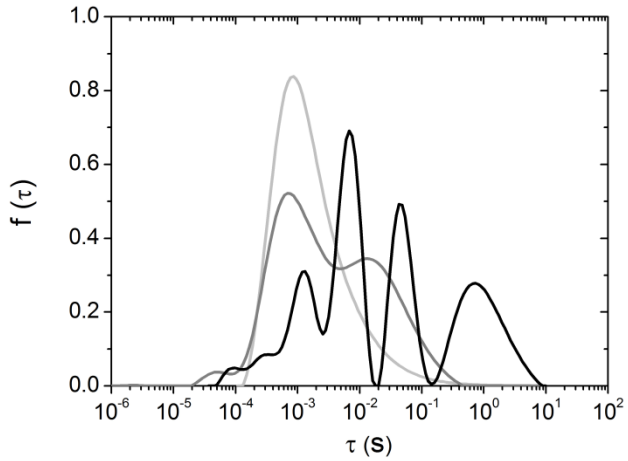

Figure 1: CONTIN analysis of the field autocorrelation functions at θ=90° from xanthan solutions of 0.03 (—), 0.6 (—) and 1.0 (—) mg/ml (with 0.03M NaCl).

This picture explains the observation of additional slower relaxation modes as concentration increases. Dynamic light scattering from complex fluids at the gel point[18] contains a power-law term for the long-time trend of the intensity auto-correlation function. As clusters are formed there is a fast mode of local cooperative fluctuations that is unperturbed by the connentivity divergence at long length scales. The latter introduces long wavelength density fluctuations that are much slower than the local cooperative diffusion. In figure 2 the double logarithmic plots reveal a power-law at long times whose slope decreases as a function of concentration. The DLS autocorrelation functions of this work was sufficiently fitted with the single component power-law function [18, 19] (equation 3). We have to note that this simple function fitted our $g_{(1)}(\tau)$ data for all angles and concentrations.

$$g_{(1)}(\tau) = (1 + \tau/\tau_{rel})^{-a} \qquad (3)$$

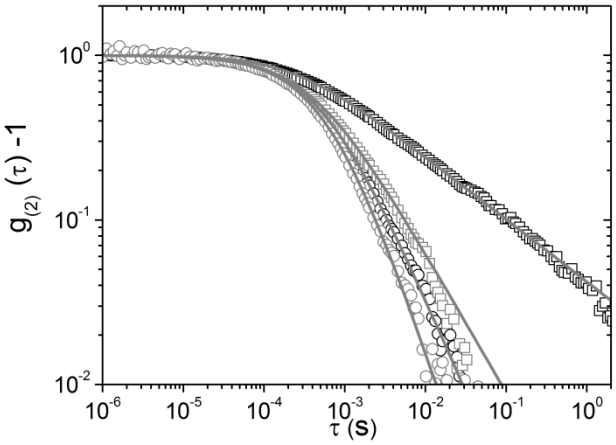

Figure 2: Intensity autocorrelation functions at θ=90° from xanthan solutions of 0.03 (○), 0.3 (○), 0.6 (□) and 1.4 (□) mg/ml (with 0.03M NaCl). Lines are fits with equation (3).

The power-law exponents a systematically decrease as concentration increases. The enhancement of elasticity at higher concentrations is this way followed by DLS[20]. Additionally we observe a q-dependence of a (figure3). At very low concentrations (up to 0.06 mg/ml) there is a low-q plateau and then a systematic increase as a function of q. Possibly at low concentration the formed clusters have smaller size than the largest length scale probed at low q and their dynamics as a whole are observed. Above 0.1 mg/ml q-dependence is systematic for all concentrations. The increase of relaxation exponent with q has been observed in gelling aqueous pluronic systems[21]. Additionally a scaling relationship[19] of the form $a = (\lambda \cdot q)^2$ has been used to model this kind of dependence in gelatin solutions and introduced a correlation length λ that decreased with concentration. This picture is qualitatively similar to our work. The power-law viscoelasticity in critical gels is connected to the power-law behaviour of the DLS correlation function[22]. Conclusively our DLS data follow the increase of the elasticity and hence are consistent with our previous work on xanthan microrheology[6].

We have to note that interchain associations in xanthan result from helix-helix associations[1] whose number possibly increases as a function of concentration. The clustering of molecules by helix-helix associations is weak and not permanent leading to the well documented shear-thinning behaviour.

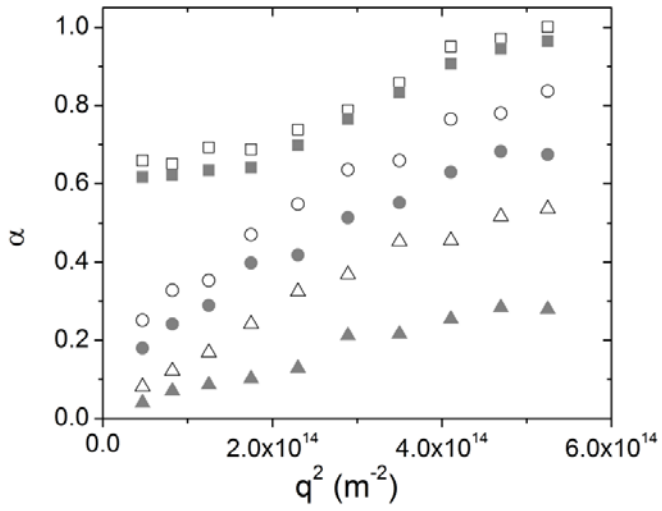

Figure 3: Characteristic relaxation exponent from xanthan solutions at 0.03 (□), 0.06 (■), 0.1 (○), 0.3 (●), 0.6 (△) and 1.4 (▲) mg/ml (with 0.03M added NaCl).

For sufficiently short times ($\tau/\tau_{rel} \ll 1$) equation 3 is written as $g_1(\tau) = 1 - \tau/(\tau_{rel}/\alpha)$ and the initial decay rate $\Gamma = \tau_{rel}/\alpha$ is extracted. It is obvious that the apparent diffusion coefficient Γ/q^2 has a strong q dependence and no systematic concentration dependence (figure 4). The $\Gamma \sim q^3$ is expected from clusters near the critical point[23] and also from Zimm model i.e. internal chain dynamics with unscreened hydrodynamic interactions. The straight line in figure 4 is the Zimm prediction[24] $\Gamma = 0.061 \cdot \frac{kT}{\eta_s} q^3$. Since xanthan solutions show self-similar properties in rheology and power law behaviour in $g_{(2)}(\tau)$ (DLS) we believe that this feature is connected to the interchain associations and not to internal Zimm dynamics.

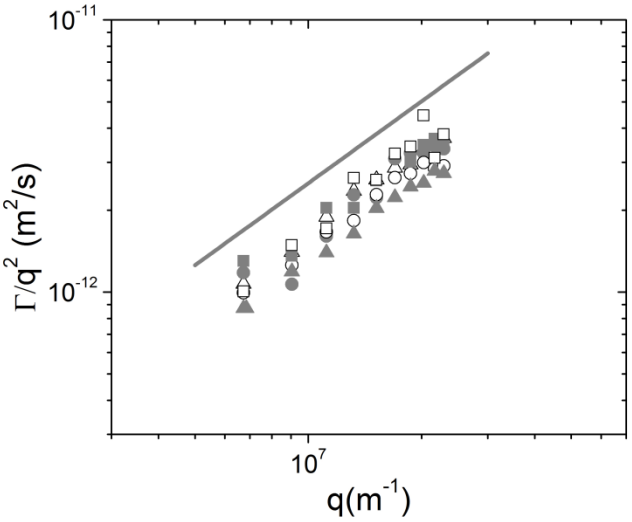

Figure 4: Apparent diffusion coefficient from xanthan solutions at 0.03 (□), 0.06 (■), 0.1 (○), 0.3 (●), 0.6 (△) and 1.4 (▲) mg/ml (with 0.03M added NaCl). Straight line is the Zimm prediction.

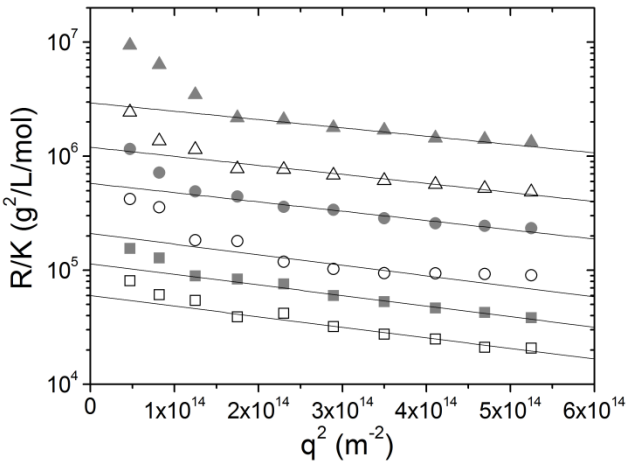

Figure 5: Guinier plots from xanthan solutions at 0.03 (□), 0.06 (■), 0.1 (○), 0.3 (●), 0.6 (△) and 1.4 (▲) mg/ml (0.03M NaCl). Lines are theoretical predictions of Guinier approximation.

The Guinier plots of xanthan solutions (figure 5) show linear trend at the most of the q-range of the SLS experiments. The straight lines are used to calculate the apparent

radius of gyration and molecular weight from equation 4 which originates from equation 1. As the extracted parameters do not present any systematic variation as concentration increases their average values are presented i.e. $R_g = 77 \pm 4\, nm$ and $M = (2.0 \pm 0.1) \cdot 10^6\, g/mol$. Xanthan in its native state prepared in unpurified commercial form has high polydispersity with an average molecular weight about 1-2·10^6 g/mol. Previous works have used fractionated and purified samples at very low concentrations to estimate the molecular weight distribution and the R_g dependence on molecular weight [7, 8]. This molecular weight of about 2·10^6 g/mol (with PDI~2) has been also reported in other works[25, 26]. The agreement with literature is remarkable since we test unfractionated solutions in the semidilute regime. The low-q upturn of the Guinier plots becomes more intense as concentration increases and reveal the structural cause (chain interconnection) of the power-law dynamics in DLS i.e. the restriction of chain dynamics at large length scales. It is in any case clear that the SLS scattering profile is dominated by the single-chain form factor for the concentrations studied by LS (up to 1.4 mg/ml).

$$\frac{R}{K} = M \cdot c \cdot exp\left(-\frac{1}{3} q^2 R_g^2\right) \qquad (4)$$

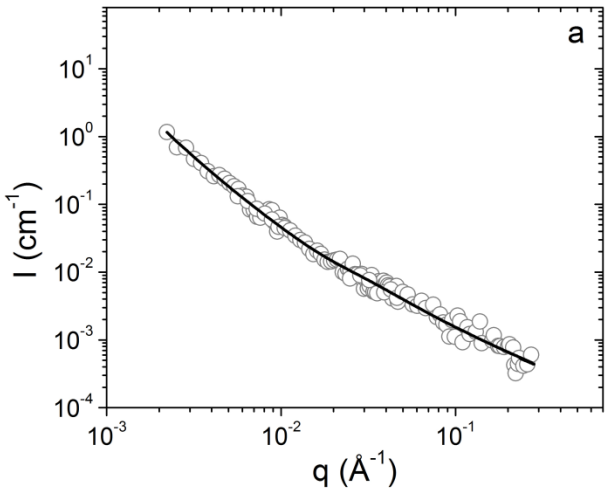

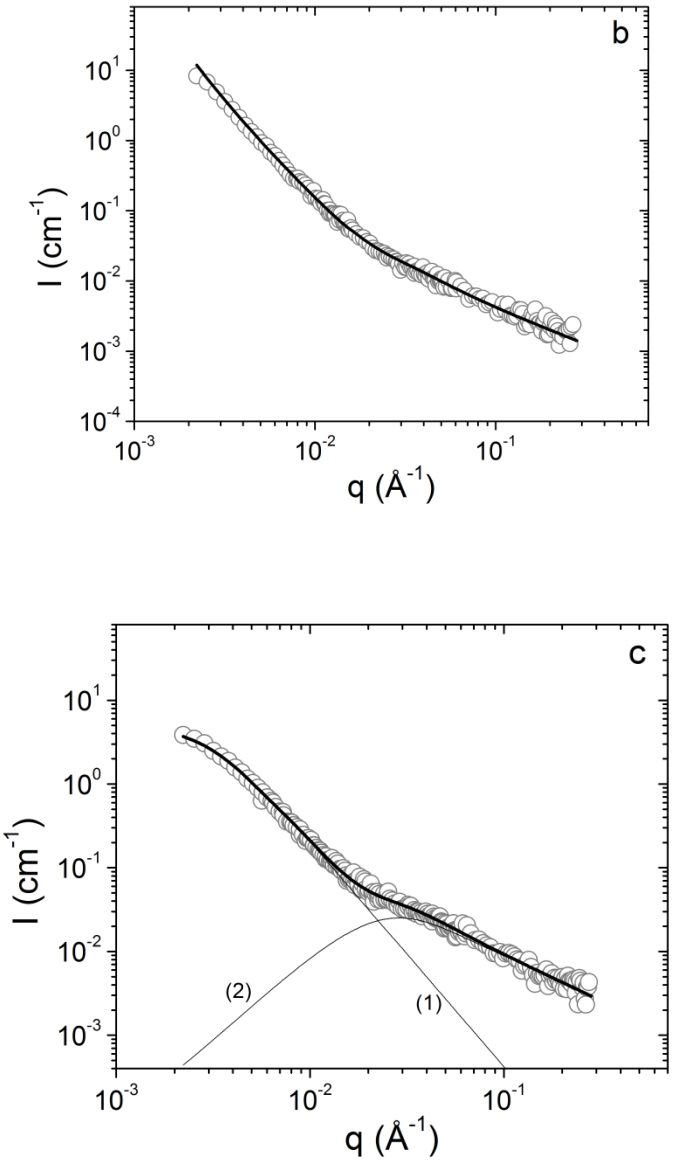

Figure 6: SANS profiles from xanthan solutions at (a) 1, (b) 3 mg/ml at 1000 rad/s and (c) 10 mg/ml at 100 rad/s with 0.03M added NaCl. Lines are fits to the data as explained in the text. In (c) the separate contributions at long (1) and short (2) length scales are shown.

We tested four concentrations of xanthan with SANS with 1 mg/ml as the lowest polymer content with adequate scattered intensity. The measurements were performed

at rest and under shear in Couette flow. Hence shear rates of 0, 10, 100 and 1000 rad/s were tested. The steady shear viscosity was consistent with the documented shear-thinning behaviour which confirmed the good shear flow conditions in our Rheo-SANS experiments (data not shown). No systematic change caused by shear flow was observed in the $I(q)$ profiles up to the highest attempted shear rate. Additionally no anisotropy was found in the 2-D $I(\vec{q})$ data. This brings two conclusions: (1) there is no flow alignment of the xanthan molecules at the length scales probed by SANS and (2) the shear-thinning properties possibly originate from the disuption of the soft helix-helix associations. Borsali et al. performed Rheo-SANS in salt-free xanthan solutions[27] at the range $0.02\ \text{Å}^{-1} < q < 0.2\ \text{Å}^{-1}$. They found a gradual increase of the SANS intensity at the polyelectrolyte peak but no shift in peak position from 500 to 12000 s^{-1}. Also anisotrpic profiles were observed under flow. Our experiments were performed in helix stabilizing salt content and consequently stronger associations would be expected in comparison to the polyelectrolyte coils in salt-free solutions. Apparently the shear alignment observed by Borsali et al. is caused by the effect of high shear rate on individual xanthan molecules.

The SANS profiles from xanthan solutions (figure 6) were insensitive to flow as discussed above and hence are presented in randomly chosen shear rates. There are two power-law regimes separated at intermediate q-range (0.02-0.03 Å^{-1}). There is a weak enhancement of scattering at the onset of the high-q power-law (0.04-0.05 Å^{-1}) mostly visible at 10 mg/ml. We have modelled the SANS data with a superposition of terms from equation 5. For the data of figure 6 we have used $I(q) = I_1(q) + I_2(q)$. The term $I_1(q)$ is the unified Beaucage model[28] where the Guinier term is bridged with the power-law term by relating the prefactors[29] G_1 and B_1. The term $I_2(q)$ is a power-law term that is modified by an error-function in order to have negligible

contributions at length scales higher than the extracted correlation length ξ i.e. at $q < 1/\xi$. For 1 and 3 mg/ml (figure 6 a and b) the low-q profile is dominated by the power-law hence no gyration radius R_{g1} can be extracted.

$$I_0(q) = B_0 \cdot q^{-D_0}$$

$$I_1(q) = G_1 \cdot exp\left(-\frac{\left(qR_{g1}\right)^2}{3}\right) + B_1 \cdot q^{-D_1} \cdot \left[erf\left(\frac{qR_{g1}}{\sqrt{6}}\right)\right]^{3D_1} \qquad (5)$$

$$I_2(q) = B_2 \cdot q^{-D_2} \cdot \left[erf\left(\frac{q\xi}{\sqrt{6}}\right)\right]^{3D_2}$$

The q range that we probed with SANS ($2\cdot10^{-3}$ - $2\cdot10^{-1}$ Å^{-1}) is at the high-q side of the range probed by LS ($6\cdot10^{-4}$ - $2\cdot10^{-3}$ Å^{-1}). Hence SANS probes the interior of xanthan coils at low concentrations (compared to the ones studied in LS) and possibly correlations between chain segments that are enhanced at higher concentrations. Slope D_1 has a value of 2 at 1 mg/ml (table 1). This is in agreement with the worm-like conformation of xanthan[8, 24]. The high-q slope D_2 is the one expected for rigid rods, is attributed to the extended helical conformation and it is the same for all concentrations within experimental error. The rigid local conformation of xanthan in the presence of salt is stabilized by the formation of hydrogen bonds between its short side chains[30]. In the case of densely grafted flexible biopolymers as aggrecan the osmotic pressure of the charged side-chains counterions preserves the polyelectrolyte character at high salt conditions[31]. If our SANS data pictured the conformation of unperturbed xanthan molecules then the characteristic q value (q^*) separating the two power-law regimes would give a rough estimation of the presistence length[32] ($6/\pi q^* \approx l_p$) with $l_p \approx 6nm$. This would be much lower than 30 nm reported by Milas for single stranded native xanthan[8]. On the other hand if ξ is used as the characteristic length scale separating the two regimes then $l_p \approx \xi = 15\,nm$ although this a crude approximation for calculating the persistence length[33].

Table 1: Extracted parameters from SANS experiments on xanthan solutions at several concentrations (with 0.03 M NaCl).

c $\left(\frac{mg}{ml}\right)$	D_0	$I(0.008\text{Å}^{-1})$ (cm^{-1})	$R_{g,1}$ (nm)	D_1	B_2 $\left(10^{-5}cm^{-1}\text{Å}^{-d_l}\right)$	ξ (nm)	D_2
1	-	0.06±0.01	-	2.0±0.1	11±1	15±3	1.00±0.01
3	-	0.31±0.02	-	2.63±0.05	41±7	13±2	0.99±0.01
8	3.3±0.2	0.49±0.01	80±3	2.76±0.05	82±4	11±1	0.99±0.01
10	3.9±0.1	0.35±0.01	57±1	2.59±0.06	107±2	9±1	1.03±0.02

The high polydispersity of xanthan solutions results from the clustering between chains. At 1 mg/ml as revealed by DLS large clusters have been already formed. At length scales higher than ξ the self-similar nature of xanthan solutions is revealed. It is a loose mass fractal at low concentrations ($D_1 = 2$) while at higher concentrations more contacts between chains form ($D_1 \approx 2.6$) as presented in table 1. This is complementary to the dynamic view from DLS. The decreasing dynamic scaling exponent (figure 3) that highlights the formation of large interconnected clusters is accompanied by the increase in the fractal exponents in the smaller length scales observed by SANS. The scaling exponents D_1 are different and hence it is not informative to compare the prefactors B_1. To compare between scattered intensity at different concentrations we present the low-q SANS intensity at a certain q i.e. 0.008 Å^{-1} (table 1). It is clear the SANS intensity at this range is not proportional to concentration (as in SLS) which is related to the change in fractal morphology and chain interconnectivity as concentration increases.

The correlation length shows a weak decrease as a function of concentration. This is a remarkable feature of the non-trivial interchain interactions. In this complex system

there must exist both overlaping and isolated chain segments at length scales up to ξ. In other words there are parts of the solution where a semidilute polyelectrolyte solution is formed and others where the chain segments are dilute. This should be the reason why xanthan solutions have shown signature of flexible linear/comb polyelectrolyte rheology[6] with simultaneous presence of self-similar complex fluid viscoelasticity. In a semidilute solution of linear or comb flexible polyelectrolytes[34, 35] the correlation length decreases as a function of concentration as $\xi \approx \left(\frac{B}{b}\right)^{1/2} \cdot c^{-1/2}$. Where b is the monomer length and B the extension parameter i.e. the contour length to chain length ratio in dilute solution. B can be defined locally as $\xi \sim g$ where g is the number of monomers within one electrostatic blob[36]. In xanthan one can definitely use $B = 1$ as will be discussed in the next paragraph. Using $b = 1\,nm$ for its monomer length[8] the scaling prediction is presented next to the experimentally observed ξ in figure 7a. The predicted values are near the observed ones but the experimental concentration dependence is weaker because of the complications introduced by the helix-helix associations. At even higher concentrations where most of the chain segments would be overlaping we would expect the ½ scaling to be recovered. The concentration dependence in figure 7a is better described as $\xi \sim c^{-1/4}$. Borsali et al.[37] have indeed observed $\xi \sim c^{-1/2}$ at higher polymer concentrations.

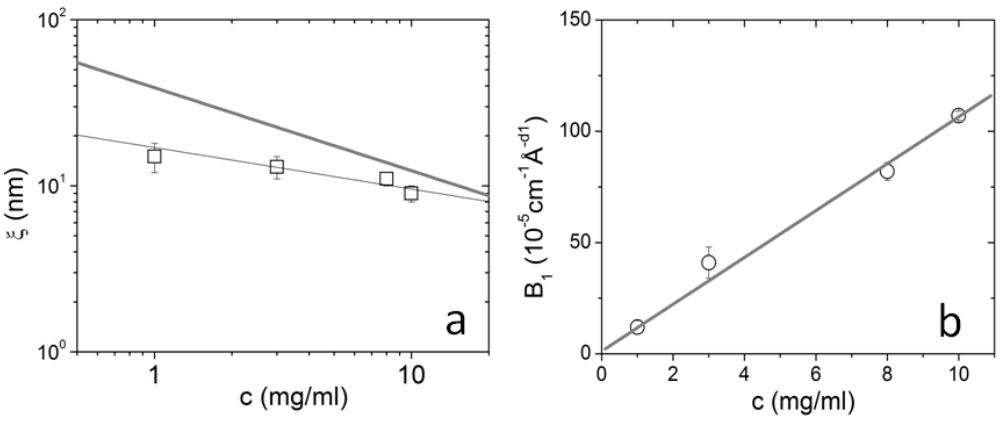

Figure 7: Correlation length (a) and scaling prefactor (b) for high q scattering obtained by SANS in xanthan solutions. Solid lines are (a) prediction for linear polyelectrolytes and (b) linear fit. Thin line in (a) is a power law with exponent -0.25.

The scaling prefactor B_2 is proportional to solution concentration obeying to $B_1 = (10.5 \pm 0.4) \cdot 10^{-5} \cdot c$ (figure 7b) confirming that the scattering at $q > 1/\xi$ comes from uncorrelated chain segments. Equation 6 can be used to estimate the molecular weight per unit length[38, 39] for xanthan. The neutron scattering length density for xanthan ($3.64 \cdot 10^{10}$ cm^{-2}) and D_2O ($6.4 \cdot 10^{10}$ cm^{-2}) were used to calculate the contrast $\Delta\rho$. In order to calculate the neutron scattering length density of xanthan we assumed all the labile protons[40] i.e. the ones in –OH groups exchanged by deuterons as has been confirmed for other polysaccharides. This treatment was also used for SANS experiments with pectin[41] and hyaluronan[42]. The mass density (d) was taken[43] as 1.67 g/ml. The resulting value was 77 ± 4 g·mol^{-1}·Å^{-1} and is comparable with the single-stranded helical morphology of native xanthan[7, 8] i.e. 98 g·mol^{-1}·Å^{-1}. The apparently lower value could be due to association of xanthan molecules by other modes than double-helix formation as multi-chain branching or randomly aggregated chain segments. This value not only reveals the expected values for the single-helix macromolecules but also the equally important fact that xanthan chains are fully stretched locally. Hence $B \approx 1$ for xanthan. Similarly cellulose[44] has been described as a locally fully stretched polyelectrolyte while flexible polyelectrolytes as linear[36] and comb[35] polystyrene sulfonate are represented by $B \approx 3$. Our data shows that the local configuration of xanthan molecules is unaltered by concentration. This supports the hypothesis that the discrepancy between the observed and the expected scaling of

the correlation lentgh is indeed connected with the complex network formation as discussed above and not with any order-disorder transition.

$$\frac{M}{L} = \frac{B_1 N_A d^2}{\pi c \Delta\rho^2} \qquad (6)$$

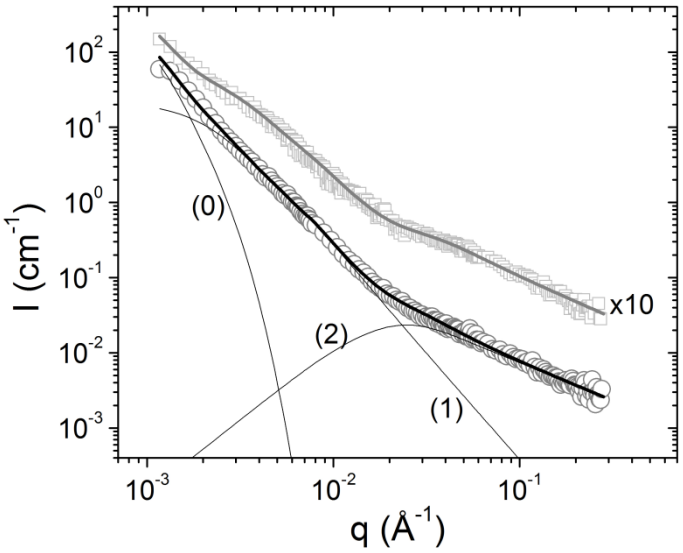

Figure 8: SANS profiles from xanthan solutions at 8 (○) and 10 (□) mg/ml for extended q range. Continuous lines are fitting curves. The separate contributions of equation 5 are shown for 8 mg/ml.

The samples of 8 and 10 mg/ml were measured by SANS at the extended q range 0.0012 - 0.3 Å^{-1}. It is clear (figure 8) that the observed Guinier-like trends at 0.002 Å^{-1} are not the signature of the largest length scale in solution. Another power-law appears and consequently the first term of equation 5 is included to model the data i.e. $I(q) = I_0(q) + I_1(q) + I_2(q)$. The resulting scaling exonents (table 1) are high (3.3±0.2 and 3.9±0.1 for 8 and 10 mg/ml respectively) signifying the formation of well-defined interfaces at large length scales.

4. Conclusions

The structural properties of native xanthan solutions in the semidilute regime were investigated by small angle neutron scattering and light scattering. At relatively low concentrations the static light scattering profiles were compatible with the expected molecular weight and gyration radius of xanthan. As concentration increased a low-q upturn highlighted the formation of helix-helix associations between separate xanthan molecules. These associations create fractal networks that are responsible for the self-similar dynamic nature of this biopolymer. The effect was observed in dynamic light scattering where the intensity autocorrelation functions showed power-law behaviour with exponents that depended on both length scale and concentration. Additionally the initial relaxation rate was not diffusive, obeyed Zimm scaling and was independent of concentration. Small angle neutron scattering probed the molecular arrangements at intermediate and short length scales. Fractal-like correlations were observed above the correlation length while the rod-like scattering at shorter length scales was used to quantify the molecular mass per unit length in xanthan. Structural arrangements and correlations did not seem to be affected by shear flow up to 1000 rad/s in the length scales probed by SANS. Consequently xanthan’s shear-thinning behaviour is connected to the breaking and re-formation of chain-chain associations and not to molecular flow alignment. This work describes the morphology and dynamics of xanthan solutions in an attempt to explain their viscoelastic properties and can be generalized to other polysaccharides.

5. Acknowledgements

Small angle neutron scattering experiments have been supported by the European Commission under the 7th Framework Programme through the 'Research Infrastructures' action of the 'Capacities' Programme, NMI3-II Grant number 283883.

References

1. G. Sworn, in *Food Stabilisers, Thickeners and Gelling Agents*, Wiley-Blackwell, 2009, DOI: 10.1002/9781444314724.ch17, pp. 325-342.
2. S. A. Frangou, E. R. Morris, D. A. Rees, R. K. Richardson and S. B. Ross-Murphy, *Journal of Polymer Science: Polymer Letters Edition*, 1982, **20**, 531-538.
3. G. Muller, M. Aurhourrache, J. Lecourtier and G. Chauveteau, *International Journal of Biological Macromolecules*, 1986, **8**, 167-172.
4. Y. Luo and Q. Wang, *International Journal of Biological Macromolecules*, 2014, **64**, 353-367.
5. B. Katzbauer, *Polymer Degradation and Stability*, 1998, **59**, 81-84.
6. A. Papagiannopoulos, K. Sotiropoulos and S. Pispas, *Food Hydrocolloids*, 2016, **61**, 201-210.
7. Y. Matsuda, Y. Biyajima and T. Sato, *Polym. J*, 2009, **41**, 526-532.
8. M. Milas, W. F. Reed and S. Printz, *International Journal of Biological Macromolecules*, 1996, **18**, 211-221.
9. P. D. Oliveira, R. C. Michel, A. J. A. McBride, A. S. Moreira, R. F. T. Lomba and C. T. Vendruscolo, *PLoS ONE*, 2013, **8**, e62713.
10. A. B. Rodd, D. E. Dunstan and D. V. Boger, *Carbohydrate Polymers*, 2000, **42**, 159-174.
11. T. A. Vilgis and H. H. Winter, *Colloid and Polymer Science*, **266**, 494-500.
12. C.-E. Brunchi, S. Morariu and M. Bercea, *Colloids and Surfaces B: Biointerfaces*, 2014, **122**, 512-519.
13. I. T. Norton, D. M. Goodall, S. A. Frangou, E. R. Morris and D. A. Rees, *Journal of Molecular Biology*, 1984, **175**, 371-394.
14. A. Papagiannopoulos, M. Karayianni, G. Mountrichas, S. Pispas and A. Radulescu, *Polymer*, 2015, **63**, 134-143.
15. B. J. Berne and R. Pecora, *Dynamic Light Scattering, With Applications to Chemistry, Biology, and Physics*, Dover, Toronto, 2000.
16. J. G. Barker and J. S. Pedersen, *J. Appl. Crystallogr.*, 1995, **28**, 105-114.
17. D. Vanderbilt and S. G. Louie, *Journal of Computational Physics*, 1984, **56**, 259-271.
18. J. E. Martin, J. Wilcoxon and J. Odinek, *Physical Review A*, 1991, **43**, 858-872.
19. S. Z. Ren, W. F. Shi, W. B. Zhang and C. M. Sorensen, *Physical Review A*, 1992, **45**, 2416-2422.
20. T. Norisuye, M. Inoue, M. Shibayama, R. Tamaki and Y. Chujo, *Macromolecules*, 2000, **33**, 900-905.
21. B. Nystrom, H. Walderhaug and F. K. Hansen, *Faraday Discussions*, 1995, **101**, 335-344.
22. T. Coviello, W. Burchard, E. Geissler and D. Maier, *Macromolecules*, 1997, **30**, 2008-2015.
23. H. C. Burstyn and J. V. Sengers, *Physical Review Letters*, 1980, **45**, 259-262.
24. W. Burchard, in *Soft Matter Characterization*, eds. R. Borsali and R. Pecora, Springer Netherlands, Dordrecht, 2008, DOI: 10.1007/978-1-4020-4465-6_9, pp. 463-603.
25. E. Pelletier, C. Viebke, J. Meadows and P. A. Williams, *Biopolymers*, 2001, **59**, 339-346.
26. N. B. Wyatt and M. W. Liberatore, *Soft Matter*, 2010, **6**, 3346-3352.
27. M. Milas, P. Lindner, M. Rinaudo and R. Borsali, *Macromolecules*, 1996, **29**, 473-474.
28. A. Papagiannopoulos, J. Zhao, G. Zhang, S. Pispas and A. Radulescu, *Polymer*, 2013, **54**, 6373-6380.
29. B. Hammouda, *Journal of Applied Crystallography*, 2010, **43**, 1474-1478.
30. W. E. Rochefort and S. Middleman, *Journal of Rheology*, 1987, **31**, 337-369.

31. A. Papagiannopoulos, T. A. Waigh, T. Hardingham and M. Heinrich, *Biomacromolecules*, 2006, **7**, 2162-2172.
32. O. Kratky, *Small-Angle X-ray Scattering*, Academic Press: New York, 1982.
33. G. Beaucage, S. Rane, S. Sukumaran, M. M. Satkowski, L. A. Schechtman and Y. Doi, *Macromolecules*, 1997, **30**, 4158-4162.
34. A. Papagiannopoulos, C. M. Fernyhough and T. A. Waigh, *The Journal of Chemical Physics*, 2005, **123**, 214904.
35. A. Papagiannopoulos, C. M. Fernyhough, T. A. Waigh and A. Radulescu, *Macromolecular Chemistry and Physics*, 2008, **209**, 2475–2486.
36. A. V. Dobrynin, R. H. Colby and M. Rubinstein, *Macromolecules*, 1995, **28**, 1859-1871.
37. M. Milas, M. Rinaudo, R. Duplessix, R. Borsali and P. Lindner, *Macromolecules*, 1995, **28**, 3119-3124.
38. Christopher B. Stanley, T. Perevozchikova and V. Berthelier, *Biophysical Journal*, 2011, **100**, 2504-2512.
39. J. S. Pedersen, *Advances in Colloid and Interface Science*, 1997, **70**, 171-210.
40. M. Gawronski, H. Conrad and T. Springer, *Macromolecules*, 1998, **31**, 2549-2551.
41. I. Schmidt, F. Cousin, C. Huchon, F. Boué and M. A. V. Axelos, *Biomacromolecules*, 2009, **10**, 1346-1357.
42. I. Morfin, E. Buhler, F. Cousin, I. Grillo and F. Boué, *Biomacromolecules*, 2011, **12**, 859-870.
43. T. Sato, T. Norisuye and H. Fujita, *Macromolecules*, 1984, **17**, 2696-2700.
44. C. G. Lopez, S. E. Rogers, R. H. Colby, P. Graham and J. T. Cabral, *Journal of Polymer Science Part B: Polymer Physics*, 2015, **53**, 492-501.